AIAA SciTech Forum
6-10 January 2025, Orlando, FL
AIAA SCITECH 2025 Forum

10.2514/6.2025-1816

Acoustic Investigation of an Implicit Characteristic Splitting Approach

Michael Pries*, Andreas Fiolitakis† and Peter Gerlinger‡
DLR, Stuttgart, Baden Württemberg, 70569, Germany

The recently developed implicit characteristic splitting (ICS) scheme has successfully been used for the computation of thermoacoustic instabilities. These kind of problems are primarily driven by the interaction of acoustic waves and the fluctuations in the heat release, possibly leading to the appearance of high pressure amplitudes. Moreover, hydrodynamic structures which can appear in the wake of a bluff body may significantly influence the establishment of a thermoacoustic feedback loop. It is therefore important to be able to not only reliably compute acoustic propagation in the linear and nonlinear regime but also successfully compute other relevant flow features with great accuracy. The focal point of this work is to investigate the ICS scheme's performance towards isolated subproblems featuring distinct acoustic and hydrodynamic aspects which need to be resolved in order to successfully compute thermoacoustic instabilities. This includes the computation of simple test cases such as one-dimensional standing wave problems, to get a better understanding of the scheme towards its dispersive and dissipative error. Besides, more complex test cases such as the Aeolian tones and the acoustics of a ducted double diaphragms flow are also considered to investigate the scheme's performance towards hydrodynamic instabilities and aeroacoustic feedback mechanisms.

I. Introduction

The reduction of pollutant emissions in modern gas turbines led to lean premixed combustion chamber concepts. These systems are known to be prone to combustion instabilities [1]. Especially thermoacoustic instabilities may inflict damage to the combustion device due to high pressure oscillations and the subsequent increased structural stress and wear. As experimental evidence emphasizes an influence of hydrogen addition on thermoacoustic instabilities, the recent trend to reduce fossil fuels in favor for hydrogen puts thermoacoustic instabilities further into focus. But, despite being a common problem during the development of new fuel flexible combustor concepts for gas turbines, the computation of thermoacoustic instabilities remains a complex and challenging task. The solution of the compressible, reacting balance and transport equations by means of large eddy simulations (LES) provides an option to compute such instabilities. Even though, as this approach obtains a solution to both, flow and acoustic fields in one computation, care must be taken to correctly capture all relevant phenomena. This is due to the discrepancies in characteristic velocities appearing between acoustic, vorticity, and entropy disturbances. While acoustic disturbances propagate with the speed of sound, vorticity and entropy disturbances are propagated with the convective velocity. In the limit of incompressible flow, at low Mach numbers, this causes a stiff system of equations where again, special care must be taken to preserve an accurate, stable, and efficient scheme [2]. The recently developed implicit characteristic splitting (ICS) scheme [3–6] has already proven its capability towards such compressible low Mach number flows. However, to efficiently and reliably compute flows prone to thermoacoustic instabilities it is important to have a thorough understanding of the scheme's capabilities towards relevant factors of influences. Among others, these are the ability to propagate small and large acoustic disturbances covering the linear as well as the non linear domain. Further, as hydrodynamic structures appearing in the flow field may significantly influence the coupling between acoustic waves and heat release fluctuations these are also relevant. Hence, the main focus of this work is to test the ICS scheme towards selected subproblems isolating distinct acoustic and flow characteristics which are relevant for the computation of thermoacoustic instabilities. These subproblems include one, two, and three-dimensional problems with increasing complexity. First, by means of a standing wave test case, the acoustic propagation under combustion chamber conditions for small and high pressure fluctuations is investigated. Next, the build up of coherent structures in the wake of the laminar flow past a cylinder is computed. The results concerning the flow as well as the acoustic field are compared against analytic, numerical, and

*Research Scientist, Institute of Combustion Technology, Computer Simulation Department
†Research Scientist, Institute of Combustion Technology, Computer Simulation Department
‡Research Scientist, Institute of Combustion Technology, Computer Simulation Department

experimental reference data. Finally, the establishment of a complex aeroacoustic feedback loop resulting in tonal noise for the ducted flow through a double diaphragm configuration is investigated. Experimental reference data is used to assess the computed results.

II. Numerical Method

The balance equations for mass, momentum, energy, and the transport equations for species mass fractions are given by (Einstein notation)

$$\frac{\partial \rho}{\partial t} + \frac{\partial \rho u_i}{\partial x_i} = 0, \tag{1}$$

$$\frac{\partial \rho u_i}{\partial t} + \frac{\partial \rho u_i u_j}{\partial x_j} - \frac{\partial \tau_{ij}}{\partial x_j} + \frac{\partial p}{\partial x_i} = \rho f_i, \tag{2}$$

$$\frac{\partial \rho E}{\partial t} + \frac{\partial u_i \rho E}{\partial x_i} + \frac{\partial u_i p}{\partial x_i} - \frac{\partial u_j \tau_{ij}}{\partial x_i} + \frac{\partial q_i}{\partial x_i} = \rho u_i f_i + S_r, \tag{3}$$

$$\frac{\partial \rho Y_\alpha}{\partial t} + \frac{\partial \rho u_i Y_\alpha}{\partial x_i} + \frac{\partial j_{\alpha i}}{\partial x_i} = S_\alpha. \tag{4}$$

In Eqs. (1)-(4), x_i are the spatial coordinates, t the physical time, ρ the density, u_i is the velocity vector, p the pressure, E is the specific total energy and Y_α the species mass fraction for the component α. The viscous stress tensor is defined through τ_{ij}, the vector of the heat flux is given by q_i, and the diffusive mass flux is $j_{\alpha i}$. Radiative and chemical sources are given by S_r and S_α whereas volume forces are denoted by f_i. The specific total energy is defined as the sum of the specific internal energy and the specific kinetic energy. A mixture of thermally perfect gases is assumed where the state equation for an ideal gas applies. Equations (1)-(4) are solved using the implicit characteristic splitting scheme (ICS) as described in [3]. Applying the ICS scheme results in (Einstein notation)

$$\frac{\rho^* - \rho^n}{\Delta t} + \frac{\partial \rho u_i}{\partial x_i} - \rho \frac{\partial u_i}{\partial x_i} = 0, \tag{5}$$

$$\frac{\rho u_i^* - \rho u_i^n}{\Delta t} + \frac{\partial \rho u_i u_j}{\partial x_j} - \rho u_i \frac{\partial u_j}{\partial x_j} - \frac{\partial \tau_{ij}}{\partial x_j} = \rho f_i, \tag{6}$$

$$\frac{\rho E^* - \rho E^n}{\Delta t} + \frac{\partial \rho u_i E}{\partial x_i} - \rho E \frac{\partial u_i}{\partial x_i} - \frac{\partial u_j \tau_{ij}}{\partial x_i} + \frac{\partial q_i}{\partial x_i} = \rho u_i f_i + S_r, \tag{7}$$

$$\frac{\rho Y_\alpha^* - \rho Y_\alpha^n}{\Delta t} + \frac{\partial \rho u_i Y_\alpha}{\partial x_i} - \rho Y_\alpha \frac{\partial u_i}{\partial x_i} + \frac{\partial j_{\alpha i}}{\partial x_i} = S_\alpha \tag{8}$$

for the advective and (Einstein notation)

$$\frac{\rho^{n+1} - \rho^*}{\Delta t} - \frac{1}{c^2}\frac{\delta p}{\Delta t} = 0, \tag{9}$$

$$\frac{\rho u_i^{n+1} - \rho u_i^*}{\Delta t} - \frac{u_i}{c^2}\frac{\delta p}{\Delta t} + \frac{\partial}{\partial x_i}\left(\frac{p^* + p^{n+1}}{2}\right) = 0, \tag{10}$$

$$\frac{\rho E^{n+1} - \rho E^*}{\Delta t} - \frac{E}{c^2}\frac{\delta p}{\Delta t} + \frac{\partial}{\partial x_i}\left(\frac{u_i p^* + u_i p^{n+1}}{2}\right) = 0, \tag{11}$$

$$\frac{\rho Y_\alpha^{n+1} - \rho Y_\alpha^*}{\Delta t} - \frac{Y_\alpha}{c^2}\frac{\delta p}{\Delta t} = 0 \tag{12}$$

for the acoustic subsystem. In Eqs. (5)-(12), c is the speed of sound, Δt denotes the discrete time step size whereas $(\cdot)^n$, $(\cdot)^*$, and $(\cdot)^{n+1}$ represent the current, intermediate, and next time levels. With $\delta p = p^{n+1} - p^*$ a pressure correction is introduced and a pressure correction equation given through (Einstein notation)

$$\begin{aligned} &\frac{\partial^2}{\partial x_i x_i}\delta p - \frac{\partial}{\partial x_i}\left(\frac{2u_i}{\Delta t c^2}\delta p\right) - \frac{4}{c^2 \Delta t^2}\delta p \\ &= -2\frac{\partial^2}{\partial x_i x_i} p^* + \frac{4}{\Delta t}\left(\frac{\rho^* + \rho^n}{2}\frac{\partial u_i^n}{\partial x_i}\right) \end{aligned} \tag{13}$$

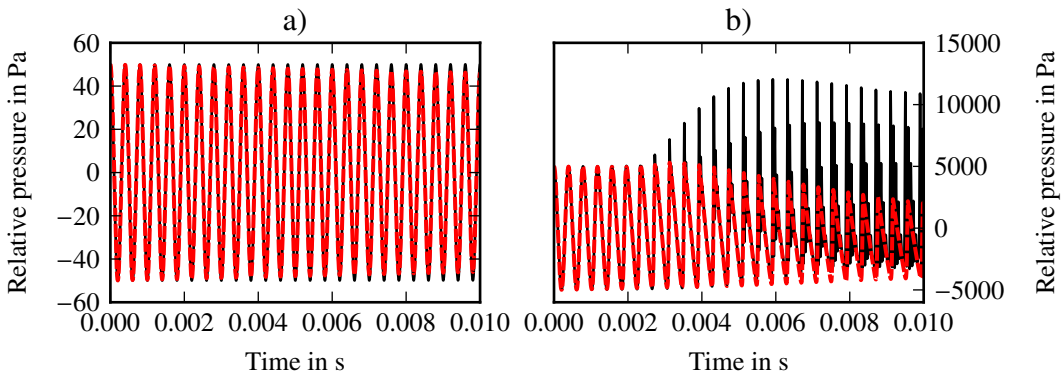

Fig. 1 Relative pressure over time for the standing wave for different dissipation settings: —— without dissipation, - - - with dissipation. a) case 1 standing wave amplitude of 50 Pa. b) case 2 standing wave amplitude of 5000 Pa.

is derived (cf. [3]). Further, numeric dissipation is introduced into the acoustic step to stabilize the solution and maintain a monotonic scheme. The advective subsystem Eqs. (5)-(8) is discretized using a temporal second order implicit Crank Nicolson scheme. Application of an implicit instead of an explicit discretization increases the stability (which is especially beneficial for numerically stiff combustion problems) but leads to a nonlinear system of equations. With the introduction of a linearization for the unknown flux and source vectors and the application of the Newton Raphson scheme a fully implicit procedure for the advective subsystem is obtained. The pressure correction equation (Eq. (13)) is also discretized in a fully implicit manner. For the pressure correction variable δp, Dirichlet boundary conditions are applied at inflows and outflows whereas at walls von Neumann boundaries are used. Subsequent to solving the pressure correction equation the solution is advanced in an explicit manner using Eqs. (9)-(12) as well as the known pressure correction variable δp. The approach is implemented in the in-house code ThetaCOM [7] using a cell-vertex [8] approach where based on a primary grid a median-dual mesh is constructed. A more detailed in-depth description of the method is given in [3].

III. Results

A. Standing wave

First, during thermoacoustic instabilities an often encountered phenomenon are standing waves. Second, the amplitudes of the pressure perturbations encountered in thermoacoustic problems may range from several hundred Pa [9] up to the order of 10^5 Pa [10]. Considering acoustic perturbations of small amplitude, the assumptions for linear acoustics hold and a propagation of the acoustic wave with insignificant attenuation is obtained. However, higher amplitudes behave differently. In case of acoustic perturbations of high amplitude, nonlinear effects such as wave steepening are observed (cf. [11, 12]). To test the ICS scheme, a one-dimensional standing wave problem with different initial pressure amplitude perturbations is considered. Solving the inviscid flow equations, the evolution of the pressure is computed over time. The one-dimensional domain has a length of $L = 0.189$ m. With a temperature of 2100 K for the gas (air, with a mass fraction for oxygen of 23% and nitrogen of 77%) at a pressure of one bar the isentropic speed of sound results in 945 m/s. An acoustic perturbation with different pressure amplitudes is initialized. In case 1 the pressure amplitudes is set to $P_A = 50$ Pa while for case 2 $P_A = 5000$ Pa is chosen. To this end, an elongated cuboid discretized with 320 hexahedral cells is used as the one-dimensional domain. The ends of the cuboid are fully reflecting free slip walls. All remaining sides of the cuboid are set to a pair of symmetry and periodic plains. The time step size of the computation is $\Delta t = 0.1$ µs. In Fig. 1a and Fig. 1b results for the pressure near a reflecting side wall are shown for the both considered cases. In each plot two results are given where additional dissipation at the correction step of the ICS scheme is applied or is not applied. For case 1 a comparatively small amplitude of $P_A = 50$ Pa is used. For this case no wave steepening is observed and the pressure waves propagate without attenuation. As can be seen in Fig. 1a the application of dissipation leads to a small attenuation of the pressure amplitude over time. For case 2 the amplitude of the pressure perturbation is set to $P_A = 5000$ Pa. In this case nonlinear effects are noticeable which lead to a wave

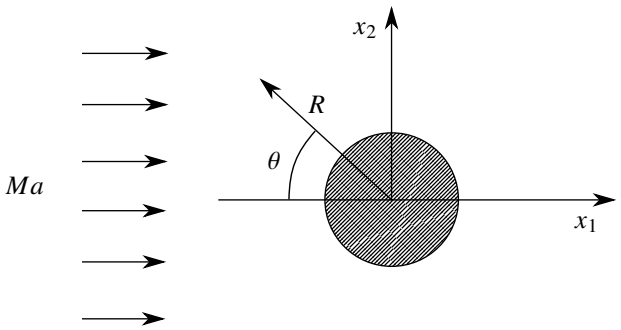

Fig. 2 Schematic drawing of the flow past a cylinder.

steepening as observed in Fig. 1b. Further, the wave is no longer isentropic as the wave amplitude is attenuated due to entropy production across the steep wave front. An additional observation is made in Fig. 1b as without additional dissipation the scheme becomes unstable and the computed solution becomes incorrect. This behavior is related to a dispersive error originated from the discretization of the pressure correction equation and needs to be accounted for in complex thermoacoustic simulations, also.

B. Aeolian tones

In common combustion chambers the flame is often stabilized by a shear layer [13–15]. Such a shear layer may be formed through a bluff body with vortices shed in its wake region. The vortices can interact with the flame, leading to heat release fluctuation causing thermoacoustic instabilities. Hence, the computation of thermoacoustic instabilities requires that the applied method is able to correctly compute such flow fields. A well studied case featuring vortex shedding is the flow past a cylinder as schematically drawn in Fig. 2. The cylinder is fixed in the origin of the x_1, x_2-plane and the R, θ-plane, respectively. In this context, R denotes the radial direction and θ is the central angle. The approaching flow is uniform as indicated in Fig. 2 by the Mach number $Ma = U_0/c_0$ with U_0 denoting the flow velocity and c_0 the speed of sound at free stream conditions. Depending on the Reynolds number given through $Re = \rho_0 U_0 D/\mu_0$, different vortex shedding modes and frequencies are possible. In this context, ρ_0 denotes the free stream density and μ_0 the dynamic viscosity. Alongside the vortex shedding an acoustic disturbance emerges known as Aeolian tone. An experimental study covering the range of $47 < Re < 2 \cdot 10^5$ is given in [16], where in the range of $47 < Re < 180$ parallel shedding under laminar flow conditions is observed. For the two-dimensional, laminar numerical investigations considered here, the Reynolds number is set to $Re = 150$ while air with a mass fraction for oxygen of 23% and nitrogen of 77% at a temperature of 293 K is used. Further, due to the small Mach numbers the fluid properties are considered to be constant where a Prandtl number of 0.75 is assumed. The inflow and outflows of the computational domain are modelled using the NSCBC approach of [17] as described in [3]. As both, the vortex shedding and the emerging acoustic perturbation are governed by the forces acting on the cylinder surface, a sufficient resolution and grid independence of the computed solution is mandatory. To obtain grid independence the focus is set first on the required resolution of the first layer height and the number of points used to resolve the cylinder. The domain size is set to $D_1 = 50D_0$ with a cylinder diameter of $D_0 = 0.005$ m and an approaching flow of $Ma = 0.2$. In the first layer the cells are almost quadratic in the x_1, x_2-plane and vary in edge length between the numerical grids. The cells adjacent to the first layer are stretched in radial direction maintaining a constant cell to cell growth rate of $\beta = 1.025$. A total of three grids are generated using different edge lengths in the first cell layer around the cylinder. The mesh number, edge length, and the resulting number of points in the primary grid are indicated in Tab. 1. Evaluated are the lift- and drag-coefficients acting on the cylinder given by $C_L = 2F_L/(U_0\rho_0 A_0)$ respectively $C_D = 2F_D/(U_0\rho_0 A_0)$, where F_D, F_L denote the drag- or lift-forces and A_0 the reference area. These coefficients are plotted in Fig. 3a for the three considered edge lengths over the dedimensionalized time. As a time scale D_0/U_0 is used, as proposed by [18]. It is observed that depending on the edge length of the first layer height the lift- and drag-coefficients slightly differ. Between mesh W1 and W2 the largest discrepancies are observed in the temporal development of the force coefficients whereas almost no difference is observed between mesh W2 and W3. Hence, for all following computations the edge length of the first layer height is set to $l_e = 5 \cdot 10^{-5}$ m corresponding to the resolution of mesh W2. Next, for this study the pressure fluctuations in the far

Mesh	l_e	Number of points
W1	$1.0 \cdot 10^{-4}$ m	54080
W2	$5.0 \cdot 10^{-5}$ m	123872
W3	$2.5 \cdot 10^{-5}$ m	283136

Mesh	$\beta_{R<100D_0}$	$\beta_{R>100D_0}$	Number of divisions	Number of points
F1	1.050	1.05	142	90376
F2	1.030	1.05	213	135248
F3	1.010	1.05	501	317264
F4	1.005	1.05	837	529616

Table 1 Computational grid parameters for evaluation of the required resolution for the cylinder (left) and the far field (right).

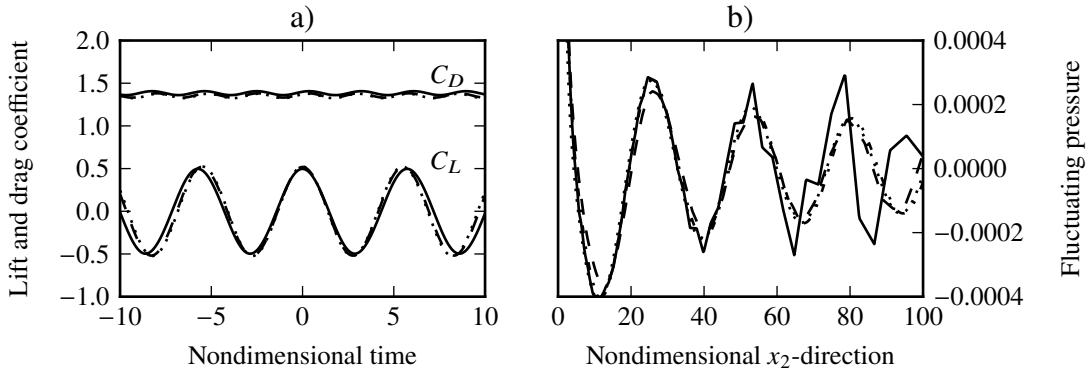

Fig. 3 Comparison of the computed solution on different computational grid configurations. a) lift C_L and drag C_D coefficients for the edge lengths —— $l_e = 1 \cdot 10^{-4}$ m, - - - $l_e = 5 \cdot 10^{-5}$ m and ····· $l_e = 2.5 \cdot 10^{-5}$ m. b) Fluctuating pressure $\Delta p'$ along $\theta = 90°$ for —— Mesh F1, - - - Mesh F2, ····· Mesh F3, -·-· Mesh F4.

field are of interest. In order to obtain an adequate resolution in radial direction four different configurations are tested. Again, an approaching flow of $Ma = 0.2$ is considered with a cylinder diameter of $D_0 = 0.005$ m. The domain size however is set to $D_1 = 200D_0$. The cell to cell growth rate in radial direction for $R < 100D_0$ is modified as indicated in Tab. 1. Further, the growth rate for $R > 100D_0$ alongside the number of divisions in radial direction and the total number of cells are given. The fluctuation pressure $\Delta p' = (p - \overline{p})/p_0$ along the positive y-direction is plotted in Fig. 3b. Here, $\overline{p}$ denotes the time average of the relative pressure p. Further, the ambient pressure is set to $p_0 = 101325$ Pa and the x_2-direction is dedimensionalized by D_0. It is seen that to obtain a sufficient resolution of the pressure in the far field mesh F3 with a cell to cell growth rate of $\beta_{R<100D_0} = 1.01$ is required. Therewith, all following computations are conducted on mesh F3. Now, analogous to [18], the Mach numbers $Ma = 0.1, 0.2$ and 0.3 are considered. According to direct numerical simulations conducted in [18], the pressure (C_p) and lift (C_L) coefficients are not affected in the considered Mach number range (Here, the pressure coefficient is evaluated as $C_p = 2p/(\rho_0 U_0^2)$). Indeed, by comparing the results for C_p plotted along the central angle θ in Fig. 4a and C_L over the dedimensionalized time in Fig. 4b the results of [18] are reproduced. Also, the qualitative increase of C_D with increasing Mach number is in accordance with the results obtained by [18]. In Tab. 2 quantitative results for the Strouhal number denoted by $St = fD_0/U_0$ with f being the shedding frequencey are given. Alongside the Strouhal number the values for the temporal average of the drag coefficient $\overline{C}_D$ together with the amplitudes for the lift and drag coefficients are noted. The amplitudes for the lift and drag coefficients are expressed by C'_D and C'_L, respectively. Comparing the obtained results given in Tab. 2 with values found in literature a very good agreement is observed. Concerning the Strouhal number the experimental investigations of [19] found a value of 0.1852 at $Re = 155$. In [16] a correlation based on experimental data is derived where for $Re = 150$ a Strouhal number of 0.1838 is obtained. Also computational studies find similar values. Examples are the incompressible flow solutions given in [20] where $St = 0.181$ and $St = 0.187$ are obtained for $Re = 140$ and $Re = 160$. Further, the incompressible study of [21] results in $St = 0.185$ at $Re = 150$. Finally, the compressible computation of [18] resulted in $St = 0.183$ for $Re = 150$. Concerning the lift and drag coefficients, at $Re = 160$ and $Ma = 0.1$ the

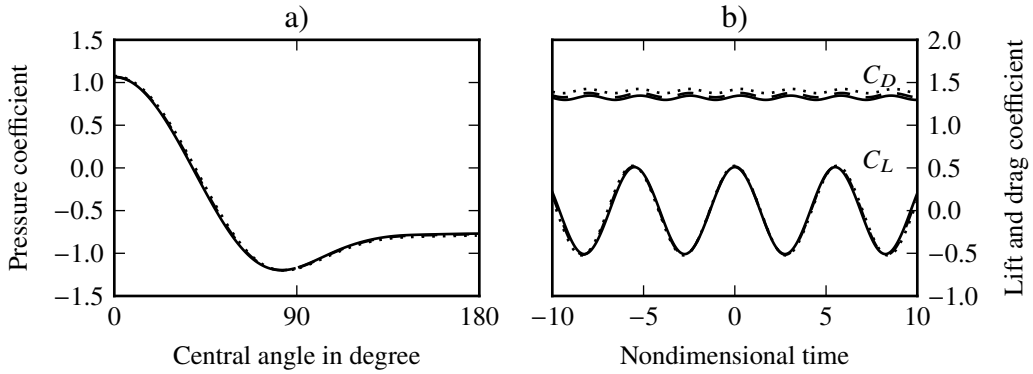

Fig. 4 Force and pressure coefficients for the Mach numbers —— $Ma = 0.1$, - - - $Ma = 0.2$, ····· $Ma = 0.3$. a) pressure coefficient C_p. b) lift C_L and drag C_D coefficients.

Ma	St	$\overline{C}_D$	C'_D	C'_L
0.1	0.181	1.32	0.025	0.509
0.2	0.181	1.35	0.025	0.514
0.3	0.180	1.40	0.025	0.525

Table 2 Resulting characteristics and coefficients for the cases: $Ma = 0.1$, 0.2 and 0.3.

incompressible computation of [20] found a time averaged drag coefficient of $\overline{C}_D = 1.32$. This coincides with [18] where the same $\overline{C}_D$ is computed except for $Re = 150$. Further, in [18] the amplitudes of the lift and drag coefficients result in $C'_D = 0.026$ and $C'_L = 0.52$. In the following, results are concerned with the far field pressure of the $Ma = 0.2$ computation. According to [22] the amplitude of a cylindrical sound pressure wave decays at large distances according to $p' \propto 1/\sqrt{R}$, where p' is the pressure amplitude and R is the radius. This is demonstrated to be valid for the here considered case of an overflown cylinder by [18] using the computed fluctuating pressure $\Delta p'$ at $Ma = 0.2$. In Fig. 5a the computed fluctuating pressure $\Delta p'$ is plotted in the same manner, along the positive x_2-direction at $\theta = 90°$ for three distinct time steps. It shows that the local minima and maxima decay with increasing radial distance. In Fig. 5b only the local maxima and minima of several discrete time steps are plotted over the radial distance R. Alongside the computed results the scaling law of [22] is plotted. The plot shows that the computed results follow the theoretical prediction confirming a correct pressure decay with increasing radial distance. By looking at Tab. 2 it can be seen that the amplitude C'_L of the lift coefficient is much larger than the amplitude of the drag coefficient C'_D. This indicates that the emerging tones are dominated by the generated lift forces acting mainly along the x_2-axis and hence, should display a dipole characteristic as shown among others in [18, 23]. For the case of $Ma = 0.2$ the root mean square of the computed fluctuating pressure is plotted along a circle with the non dimensional radius $R = 75$ in Fig. 6. It is readily seen that the emitted computed fluctuating pressure shows the expected dipole characteristic representing two lobes extending in the negative and positive x_2-direction.

C. Double diaphragms

Another mechanism that may establish an aeroacoustic or thermoacoustic feedback loop is the generation of acoustic disturbances following the impingement of vortical structures at structural parts. These acoustic disturbances may travel upstream and interact either with the generation of the vortical structures or the oxidizer and fuel mass flows leading to heat release fluctuations, thus generating a feedback loop. In the aeroacoustic case, such mechanisms are often encountered. Examples are the self sustaining oscillations of flows over cavities [24, 25] and the flow through two ducted diaphragms [26–31]. Since thermoacoustic instabilities occur usually in confined flows the latter case is of more interest here. At the *Ecole Centrale de Lyon* (France) such a case has been experimentally studied providing wall pressure as well as velocity data by means of microphone and Laser Doppler Anemometry (LDA) measurements. A

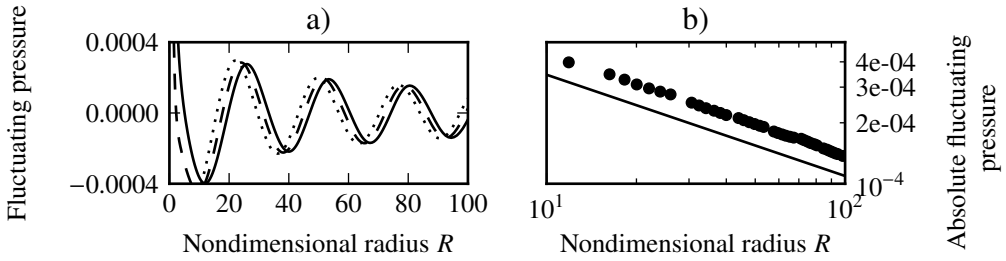

Fig. 5 Fluctuating pressure along $\theta = 90°$ for $Ma = 0.2$. a) fluctuating pressure $\Delta p'$ at —— $t = 10250$, - - - $t = 10255$, ····· $t = 10260$. b) absolute values of the computed (•) local minimal and maximal fluctuating pressure $|\Delta p'|$ together with the analytic scaling law (——).

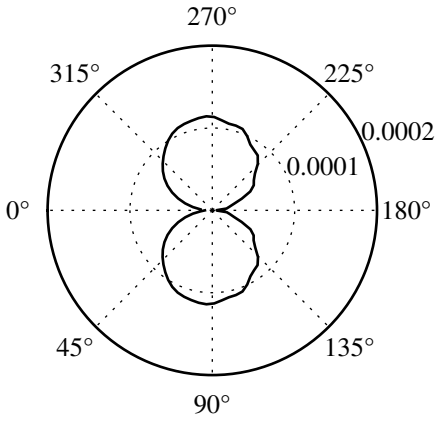

Fig. 6 Root mean square of the fluctuating pressure $\Delta p'_{\mathrm{RMS}}$ along a circle with the non dimensional radius $R = 75$ at $Ma = 0.2$.

schematic view of the configuration used in the measurements is given in Fig. 7 where the flow direction is from left to right. An important aspect of this case is that depending on the distance of the two diaphragms, a feedback loop between vortex creation at the first diaphragm and vortex impingement at the second diaphragm connected through an upstream travelling acoustic disturbance establishes. This feedback loop results in an acoustic resonance recognized as a tone at a distinct frequency. In the measurement campaign two diaphragm distances are investigated. For case 1 $L = 2R$ is applied where acoustic resonance is observed. No resonance is obtained for case 2 with $L = 4R$ where R denotes the duct radius. The inflow velocity measured far upstream of the diaphragms is $U = 5.4\,\mathrm{m/s}$ and is considered to be fully developed. In order to reduce acoustic ambient noise and undesired reflection the inflow and outflow were treated accordingly. The resulting wall pressure is measured at five and the velocity profiles at eleven different locations upstream, between, and downstream of the two diaphragms. For further details considering the experimental setup, the studies in [31] may be consulted. Additionally, in [31] numerical investigations by means of LES are presented. Analogous to [31] both cases are investigated here by means of LES applying the ICS scheme. To this end the system of equations presented in Sec. II is solved in its Favre filtered form. The arising subgrid-scale stress tensor is closed using the wall-adapting local eddy-viscosity (WALE) model of [32]. If not noted otherwise, the WALE constant is set to $C_W = 0.2$. To close the subgrid-scale energy fluxes a gradient diffusion approach is used relating the fluxes to the Favre filtered temperature gradient. Considering the computational domain, in both configurations, case 1 ($L = 2R$) and case 2 ($L = 4R$), the inflow and outflow is located $14R$ away from the upstream respectively downstream diaphragm. Such a large domain is chosen to minimize possible residuary disturbances due to inaccuracies emerging at the inflow and

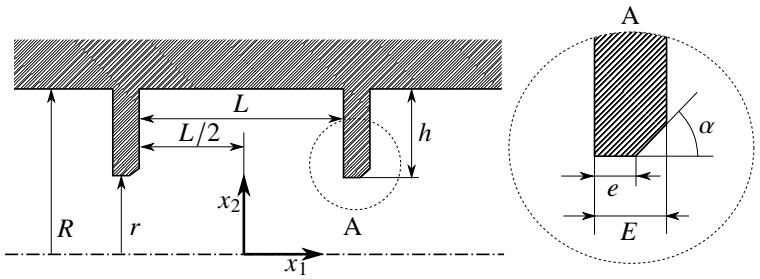

Parameter	Value
R	25.00 mm
r	14.00 mm
h	11.00 mm
E	1.98 mm
e	0.90 mm
α	17.90°
L	$2R$ / $4R$

Fig. 7 Schematic drawing of double diaphragm test case.

σ_2 [kg/(s^{3}mK)]	$\sigma_{3,4}$ [1/s]	σ_5 [kg/(m^{2}s^2)]	σ_6 [1/s]
$1.5 \cdot 10^5$	$2.5 \cdot 10^5$	$2.5 \cdot 10^5$	$1.5 \cdot 10^5$

L_{out} [m]	Ma_{out}	σ_{out}	p_{out} [Pa]
0.05	0.015	0.075	101325

Table 3 NSCBC parameters for inflow (left) and outflow (right) of the double diaphragms test case.

outflow boundaries which could impair the phenomenons generated by the diaphragms. The inflow respectively outflow is modelled as partially reflective using the NSCBC approach of [17] as described in [3] where the parameters are listed in Tab. 3. Here, the parameters σ_{2-6} are case dependent constants defining the relaxation parameters associated with a subsonic partially reflecting inflow as defined in [31]. Analogously, the outflow parameters are used to define the subsonic partially reflecting outflow where the relation of [33] given by $K = \sigma_{\text{out}}(1 - Ma_{\text{out}})c/L_{\text{out}}$ is used. Here, K defines the relaxation parameter at the outflow boundary while Ma_{out}, σ_{out}, and L_{out} are the case dependent Mach number, relaxation parameter, and characteristic length used to define the outflow boundary. In the experimental investigations also the reflection coefficients of the test facilities inflow and outflow have been characterized. A direct comparison of the reflection coefficients with the numerical setup for the longitudinal waves according to [3] is plotted in Fig. 8. At the inflow a fully developed turbulent flow profile without turbulent fluctuations, following the one-seventh power law with a maximal velocity of $U_{\text{in}} = 5.4\,\text{m/s}$ is assumed. As fluid, air with a mass fraction for oxygen of 23% and nitrogen of 77% at the inflow temperature of $T_{\text{in}} = 290.65\,\text{K}$ is applied. For the encountered phenomenon not only the acoustic disturbances need to be well resolved but also a correct build up and transport of the vortical structures is required. A hybrid meshing approach is used for this reason for the primary grid where the areas confined by the diaphragms is meshed using hexahedral cells. Cell agglomeration is applied towards the mouths of the diaphragms. Outside the area confined by the diaphragms, tetrahedral cells are applied with successive coarsening towards the inflow and outflow of the computational domain to favor numerical dampening of inaccuracies due to unwanted reflections at the inflow and outflow. To assure a sufficient resolution of both mechanisms three different numerical grids are tested for case 1. For these meshes the number of control volumes in the median-dual mesh is varied between 1.7, 5.1, and

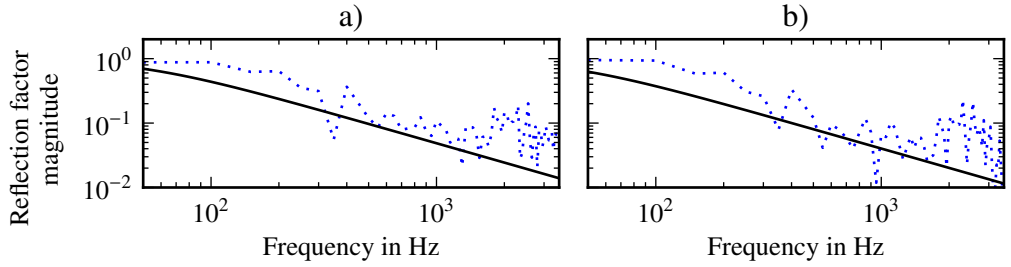

Fig. 8 Comparison of reflection factors for inflow (a)) and outflow (b)). —— computation, ····· measurement.

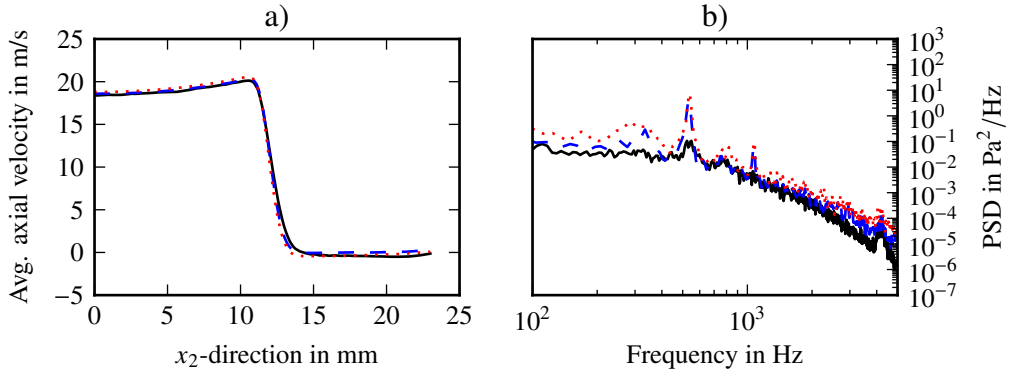

Fig. 9 Comparison of computational grids for case 1. a) averaged axial velocity at $x_1 = -20$ mm, b) Power spectral density of the wall pressure at $x_1 = 0$ mm. —— coarse, - - - medium, ····· fine.

14.0 million for the coarse, medium, and fine grid. In Fig. 9 the computed averaged axial velocities as well as the power spectral densities (PSD) for case 1 on the different numerical grids are plotted. Comparing the averaged axial velocity profiles in Fig. 9a plotted at $x_1 = -20$ mm it is seen that the differences between the three tested grid resolutions is small. This indicates that concerning the averaged velocity field, a sufficient resolution is already obtained by the coarsest grid. However, considering the acoustic pressure by looking at the PSD of the wall pressure at $x_1 = 0$ mm given in Fig. 9b a different behaviour is obtained. Starting with the coarse grid a first small peak is observed at a frequency of $f = 535$ Hz. Towards higher frequencies the spectrum decreases monotonically until $f = 4160$ Hz where a second peak is observed. The results concerning the PSD of the wall pressure on the medium and fine sized grids differ. Here, a first broad peak is observed at around $f = 317$ Hz followed by a pronounced peak at $f = 538$ Hz and a smaller one at $f = 1075$ Hz. After that the spectrum monotonically decreases until $f = 4160$ Hz where as compared to the coarse solution a fourth peak appears. Comparing the amplitudes it is seen that the monotonic decrease towards heigh frequencies is largest for the coarse grid and smallest for the fine grid. The medium sized grid lies in between. As all computational parameters are kept constant, these discrepancies for the monotonic decrease are related to the different mesh resolutions and the entailed differences in the numerical dissipation. Next, a closer look is taken on the peaks at frequencies $f = 538$ Hz and $f = 1075$ Hz. These peaks are of most interest as they are associated with the acoustic modes occurring at case 1. Only for the medium and fine sized grids significant amplitudes at these frequencies are observed where slightly higher values are obtained for the fine grid. This results in the observation that, as compared to the averaged velocity field, the obtained wall pressure is much more sensitive towards the resolution of the computational grid. Further, it requires at least the medium sized grid to establish the aeroacoustic feedback loop between shedding, impinging, and upstream traveling pressure wave. Due to the slightly higher wall pressure amplitudes, the solution on the fine grid is used for the following analyses. Also, all further computations are computed on numerical grids using the fine grid settings.

D. Case 1

A comparison between the computationally and experimentally achieved results for case 1 is given in Fig. 10. Compared are the average axial velocity as well as the root mean squares of the velocity fluctuations at different locations along the streamwise direction x_1. The positions of the profiles are indicated in the figure. Further, a comparison of the resulting power spectral densities of the computational and experimental findings at $x_1 = -82$ mm, $x_1 = 0$ mm, and $x_1 = 82$ mm is given. Relating the averaged axial velocity profiles overall a very good agreement is obtained. Only slight deviations are observed directly downstream of the first diaphragm where the flow accelerates as a result of the provoked flow restriction. This is best visible at $x_1 = -20$ mm. Here, the computed result obtains slightly higher flow velocities between -10 mm $< y < 10$ mm as compared to the measurements. This is a direct result due to mass conservation. The small misalignment of the slopes at $x_2 = \pm 12$ mm lead to a narrower cross section in the computational results causing higher axial flow velocities. The increased velocities in the core flow persist between the two diaphragms up until $x_1 = 30$ mm. Further downstream, the deviation in the core flow velocities reduces and the computed and experimental values are in an excellent agreement. Similar observations are made for the RMS of the velocity fluctuations. Here,

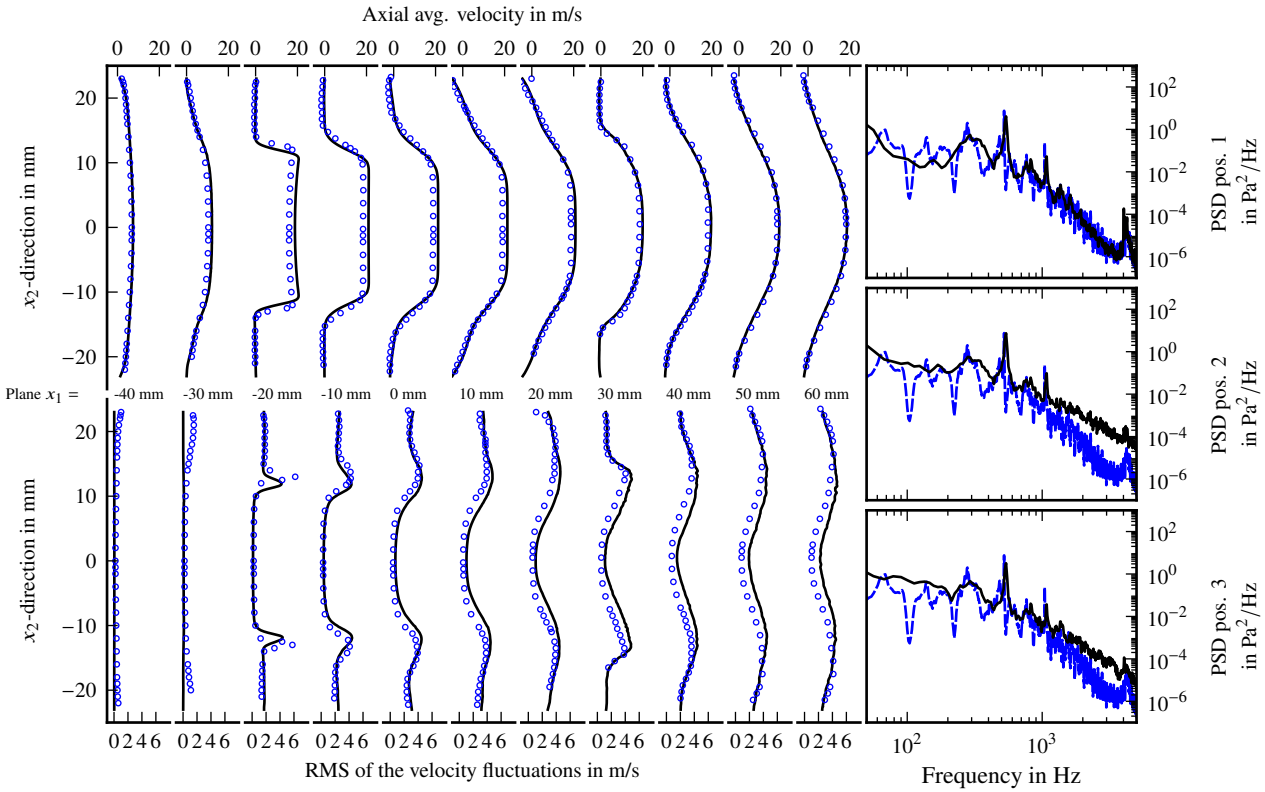

Fig. 10 Comparison of the experimentally and numerically (C_W = 0.2) obtained averaged velocity, the root mean square of the velocity fluctuations as well as power spectral density of the wall pressure for case 1. Position of microphones are: pos. 1 $x_1 = -82$ mm, pos. 2 $x_1 = 0$ mm, and pos. 3 $x_1 = 82$ mm. —— numerical, - - - and ○ experimental.

upstream the first diaphragm at $x_1 = -40$ mm and $x_1 = -30$ mm differences between the computed and measured values only exist towards the duct walls where higher fluctuations are obtained in the experimental results. As a smooth profile without turbulent fluctuations is imposed for the simulation, this deviations are expected. At $x_1 = -20$ mm two distinct peaks are visible in the RMS velocity fluctuation profile at $x_2 = \pm 12$ mm. The position and the magnitude slightly deviate between computation and experiment. For the magnitude, the simulation obtains lower values whereas the deviation in position fits the misalignment of the slopes in the averaged velocity profile at the same location. Further downstream, at $x_1 = -10$ mm up to $x_1 = 20$ mm, the numerical solution compares well with the experimental measurements in terms of qualitative and quantitative agreement. Downstream the second diaphragm beginning with $x_1 = 30$ mm, the computed solution obtains larger fluctuations in the core flow region for -13 mm $< y < 13$ mm as compared to the experimental values. Referring to the acoustic pressure, wall pressure measurements upstream, between and downstream the diaphragm section are available and compared against the numerical results, also. A very good agreement in terms of frequency and amplitude of the occurring peaks at $f = 325$ Hz and $f = 1048$ Hz is achieved at all three positions. However, slight differences exist. First, the frequency of the first peak for the computational result is 12 Hz higher as compared to the measurements. Consequently, also an increased frequency in the computational results is observed in the second peak, being the higher harmonic of the first peak. One reason may be a deviation in the geometrical setup, as the experiment is prone to manufacturing tolerances. Another uncertainty adding to a deviation in frequency could be a slightly different speed of sound due to differences in fluid properties as compared to the experiment. Aside of the frequencies, in the simulation, the amplitudes are somewhat lower as compared to the experimental findings. This is more pronounced for the higher harmonic ($f = 1048$ Hz) at position one and three. The small increase in deviation of the amplitudes is related to an increased dampening caused by the larger numerical dissipation following the coarser grid settings upstream and downstream the diaphragms. Comparing the decrease in the

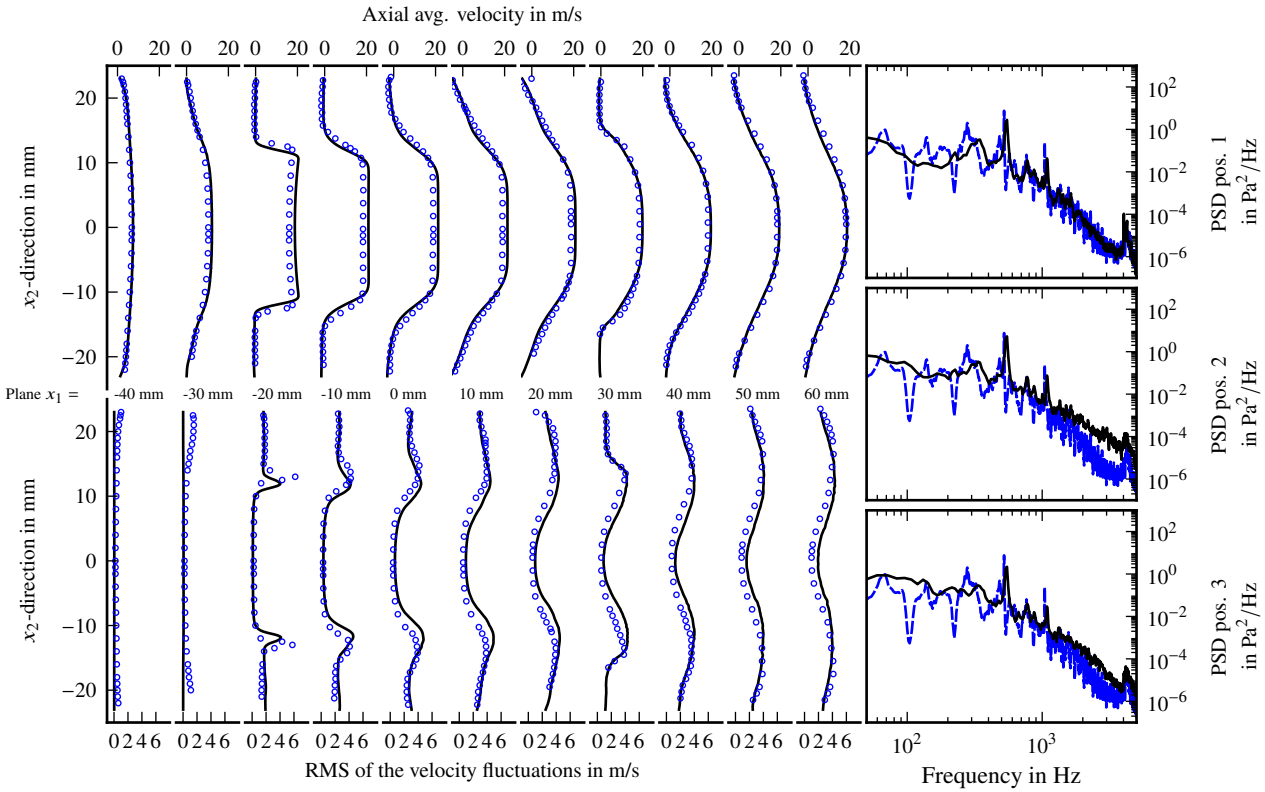

Fig. 11 Comparison of the experimentally and numerically ($C_W = 0.6$) obtained averaged velocity, the root mean square of the velocity fluctuations as well as power spectral density of the wall pressure for case 1. Position of microphones are: pos. 1 $x_1 = -82$ mm, pos. 2 $x_1 = 0$ mm, and pos. 3 $x_1 = 82$ mm. —— numerical, - - - and ○ experimental.

pressure spectrum at high frequencies this assumption is encouraged, where the largest discrepancies are observed for position two with the highest grid resolution. The inaccurate decrease in the wall pressure spectrum for high frequencies especially visible at position two between the diaphragms may indicate that the dissipation of energy is not correctly modelled in the computation. As mainly high frequencies are affected, this may be related with an erroneous dissipation of kinetic energy related with the small turbulent scales. Using the WALE model, the dissipation of kinetic energy on subgrid level is adjusted by the case dependent WALE constant C_W. One way to increase the dissipation towards smaller turbulent scales is to adjust this constant. For this reason a computation on the fine grid with $C_W = 0.6$ is conducted. The results for this computation in terms of averaged velocity profiles, the profiles for the RMS of the velocity fluctuations, and the wall pressure spectra are given in Fig. 11. It is readily seen that as compared to the results with $C_W = 0.2$ the decrease in the wall pressure spectrum of position two and three towards high frequencies is better matched for the results with $C_W = 0.6$. At position three, the experimental fall off in the spectrum is almost achieved whereas at position two a deviation compared to the experimental data is still well visible. The already very good results at position one remain unchanged. Also, the frequencies of the acquired peaks are not influenced. However, comparing the amplitudes of the peaks, slightly lower values are obtained for the computation with $C_W = 0.6$. Further, by comparing the averaged velocity profiles no significant differences are observed compared to the results obtained with $C_W = 0.2$ and the overall agreement with the experimental data is maintained. In contrast, for the RMS of the velocity fluctuations small differences between the computation with $C_W = 0.2$ and $C_W = 0.6$ are observed. These differences are obtained at $x_1 = -20$ mm and downstream the second diaphragm at $x_1 = 40$ mm to $x_1 = 60$ mm. At $x_1 = -20$ mm the magnitude of the two observed peaks at $x_2 = \pm 12$ mm is getting smaller in the $C_W = 0.6$ case. A similar behaviour is seen in the core flow in the profiles at $x_1 = 40$ mm to $x_1 = 60$ mm where the overestimation of the fluctuations compared to the experimental results is reduced.

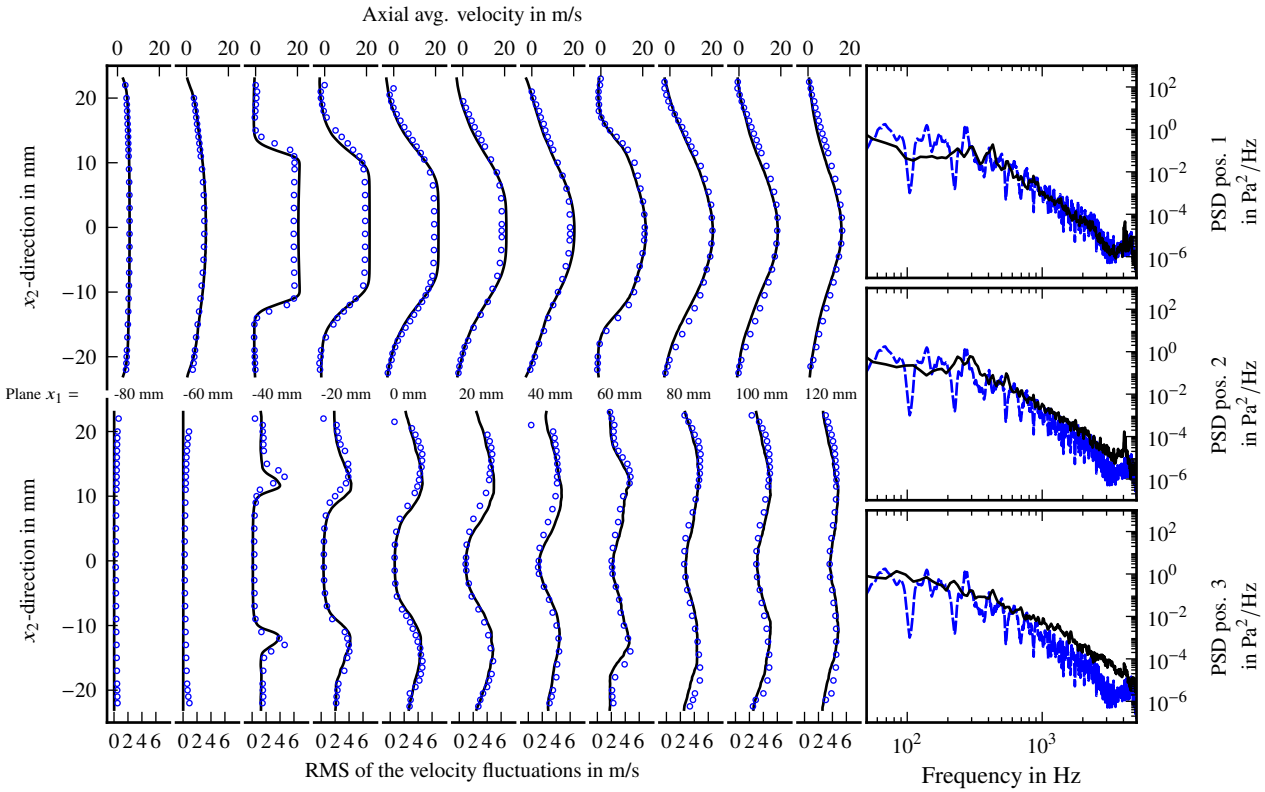

Fig. 12 Comparison of the experimentally and numerically (C_W = 0.6) obtained averaged velocity, the root mean square of the velocity fluctuations as well as power spectral density of the wall pressure for case 2. Position of microphones are: pos. 1 $x_1 = -107$ mm, pos. 2 $x_1 = 0$ mm, and pos. 3 $x_1 = 107$ mm. —— numerical, - - - and ○ experimental.

E. Case 2

Next, case 2 is investigated. This case differs from case 1 by a doubled distance between the diaphragms. For this case, no pronounced aeroacoustic resonance is measured in the experiments. The fine settings are used for the computational model leading to a total number of control volumes in the median-dual grid of about 21 millions. The WALE constant is set to $C_W = 0.6$. Again, in Fig. 12 a comparison of the averaged axial velocities, the RMS of the fluctuating velocities, and the PSD of the wall pressure is given. The positions along the streamwise direction for the velocity profiles are indicated in the figure, whereas the wall pressure measurements are given at $x_1 = -107$ mm, 0 mm, and 107 mm which are referred to as position one, two, and three. For the averaged axial velocities, as for case 1, an overall excellent agreement is obtained. Slight deviations only exist downstream the first diaphragm where the velocities in the core flow are somewhat higher compared to the experimental findings. Again, this results from the small mismatch in the location of the slopes best visible at $x_1 = -40$ mm. Also the computed profiles for the RMS of the fluctuating axial velocities are in a very good agreement with the measurements. As expected from the smooth inflow profile without imposed turbulent fluctuations, far upstream at $x_1 = -80$ mm and $x_1 = -60$ mm small differences are visible. At $x_1 = -40$ mm the bulges are slightly shifted towards the centreline as compared to the experiment. This follows the trend of the slight misalignment of the slopes observed in the averaged axial velocity profile at the same position. Nevertheless, the amplitude of the bulges are well matched. Downstream the second diaphragm starting at $x_1 = 60$ mm the differences in axial velocity fluctuations between computed and measured solution are negligible. Comparing the PSD of the computed and measured wall pressures at positions one, two, and three it is apparent, that no aeroacoustic resonance is obtained in the computed data which is in agreement with the experimental findings. Moreover the decay in the wall pressure spectrum is excellent at position one and only slightly overestimated at position two and three indicating an overall correct behaviour of the computational model.

IV. Summary and Conclusion

The complex mechanism leading to thermoacoustic interactions involves multiple different physical phenomenons interacting with each other. This introduces difficulties understanding erroneous computational results not aligning with experimental findings or numeric reference data. To get a reliable solution towards thermoacoustic instabilities it is a minimal requirement to obtain reliable and accurate solutions to the contributing subproblems. For this reason, contributing mechanisms are identified and investigated separately by means of three different test cases with increasing complexity. First, due to the high pressure amplitudes frequently encountered in thermoacoustic problems the acoustic waves are subject to nonlinear effects such as wave steepening. This wave steepening leads to entropy production and the initiated sinusoidal wave degenerates to a damped saw tooth signal. Unless introducing additional numerical damping, the solution computed with the ICS scheme becomes unstable introducing parasitic modes due to dispersive errors. Second, the ICS scheme's ability to compute coherent hydrodynamic structures in combination with the associated acoustic fields is demonstrated. These flow structures are of great significance in the mechanisms driving thermoacoustic instabilities. The flow past a cylinder shows that for the correct representation of the unsteady flow features a high spatial resolution around the cylinder is required. Also, for a correct representation of the acoustic field a high spatial resolution in the region of interest is necessary. Referring to common combustion chambers, this indicates that a sufficiently high grid resolution not only in the combustion zone is required but also throughout the domain where reflected acoustic waves may interfere with the flow features. A similar observation is made for the ducted double diaphragm test case, where a resonant feedback cycle only occurs if all flow and acoustic features are sufficiently resolved. Again, referring to combustion chambers, there is also a need for an adequate resolution which resolves downstream traveling coherent structures without excessive dampening. Overall, if all requirements are met, the ICS scheme does show a very good ability to compute problems primarily associated with aeroacoustic.

Acknowledgments

The authors would like to thank Alois Sengissen for providing valuable experimental reference data concerning the ducted double diaphragms case. Further, we gratefully acknowledge the scientific support and HPC resources provided by the German Aerospace Center (DLR). The HPC system CARA is partially funded by "Saxon State Ministry for Economic Affairs, Labour and Transport" and "Federal Ministry for Economic Affairs and Climate Action". The HPC system CARO is partially funded by "Ministry of Science and Culture of Lower Saxony" and "Federal Ministry for Economic Affairs and Climate Action".

References

[1] Dowling, A. P., and Hubbard, S., "Instability in Lean Premixed Combustors," *Proceedings of the Institution of Mechanical Engineers, Part A: Journal of Power and Energy Volume 214, Issue 4*, 2000, pp. 317–332. doi:10.1243/0957650001537903.

[2] Choi, D., and Merkle, C., "Application of Time-Iterative Schemes to Incompressible Flow," *AIAA Journal*, Vol. 23, No. 10, 1985, pp. 1518–1524. doi:10.2514/3.9119.

[3] Pries, M., Fiolitakis, A., and Gerlinger, P., "An Implicit Splitting Scheme with Characteristic Boundary Conditions for Compressible Reactive Flows on Unstructured Grids," *Journal of Computational and Applied Mathematics*, Vol. 437, 2024, p. 115446. doi:10.1016/j.cam.2023.115446.

[4] Fiolitakis, A., and Pries, M., "A Novel Approach to the Characteristic Splitting Scheme for Mildly Compressible Flows Based on the Weighted Averaged Flux Method," *Journal of Computational Physics*, Vol. 513, 2024, p. 113197. doi:10.1016/j.jcp.2024.113197.

[5] Pries, M., Fiolitakis, A., Hadef, R., and Gerlinger, P., "Numerical and Experimental Investigation of Self Excited Thermoacoustic Instabilities in a Lean, Partially Premixed Swirl Flame," *AIAA SCITECH 2024 Forum*, 2024. doi:10.2514/6.2024-0592, No.: AIAA-2024-0592.

[6] Fiolitakis, A., Pries, M., Lammel, O., and Kathrotia, T., "Investigation of High-Frequency Thermoacoustic Instabilities in a FLOX® Burner Using Large-Eddy Simulation and Multi Resolution Proper Orthogonal Decomposition," *AIAA SCITECH 2024 Forum*, 2024, pp. 1–16. doi:10.2514/6.2024-0794, No.: AIAA-2024-0794.

[7] Setzwein, F., Ess, P., and Gerlinger, P., "An Implicit High-Order k-Exact Finite-Volume Approach on Vertex-Centered Unstructured Grids for Incompressible Flows," *Journal of Computational Physics*, Vol. 446, 2021, p. 110629. doi:10.1016/j.jcp.2021.110629.

[8] Barth, T., and Jespersen, D., "The Design and Application of Upwind Schemes on Unstructured Meshes," *27th Aerospace Sciences Meeting*, 1989. doi:10.2514/6.1989-366.

[9] Hantschk, C.-C., and Vortmeyer, D., "Numerical Simulation of Unsteady Interaction between Flow, Heat Conduction and Acoustics within a Rijke Tube," *Chemical Engineering & Technology*, Vol. 23, No. 9, 2000, pp. 758–763. doi: 10.1002/1521-4125(200009)23:9%3C758::AID-CEAT758%3E3.0.CO;2-U.

[10] Smith, J., Klimenko, D., Clauss, W., and Mayer, W., "Supercritical LOX/Hydrogen Rocket Combustion Investigations Using Optical Diagnostics," *38th AIAA/ASME/SAE/ASEE Joint Propulsion Conference & Exhibit*, 2002. doi:10.2514/6.2002-4033, No.: AIAA-2002-4033.

[11] Morse, P. M., and Ingard, K., *Theoretical Acoustics*, Princeton university press, 1986.

[12] Baum, J., and Levine, J. N., "Numerical Techniques for Solving Nonlinear Instability Problems in Solid Rocket Motors," *AIAA Journal*, Vol. 20, No. 7, 1982, pp. 955–961. doi:10.2514/3.7957.

[13] Longwell, J. P., Frost, E. E., and Weiss, M. A., "Flame Stability in Bluff Body Recirculation Zones," *Industrial & Engineering Chemistry*, Vol. 45, No. 8, 1953, pp. 1629–1633. doi:10.1021/ie50524a019.

[14] Davies, T. W., and Beér, J. M., "Flow in the Wake of Bluff-Body Flame Stabilizers," *Symposium (International) on Combustion*, Vol. 13, No. 1, 1971, pp. 631–638. doi:10.1016/S0082-0784(71)80065-6.

[15] Coats, C. M., "Coherent Structures in Combustion," *Progress in Energy and Combustion Science*, Vol. 22, No. 5, 1996, pp. 427–509. doi:10.1016/S0360-1285(96)00011-1.

[16] Fey, U., König, M., and Eckelmann, H., "A new Strouhal-Reynolds-Number Relationship for the Circular Cylinder in the Range $47 < \mathrm{Re} < 2\mathrm{x}10^5$," *Physics of Fluids*, Vol. 10, No. 7, 1998, pp. 1547–1549. doi:10.1063/1.869675.

[17] Poinsot, T., and Lele, S., "Boundary Conditions for Direct Simulations of Compressible Viscous Flows," *Journal of Computational Physics*, Vol. 101, No. 1, 1992, pp. 104–129. doi:10.1016/0021-9991(92)90046-2.

[18] Inoue, O., and Hatakeyama, N., "Sound Generation by a Two-Dimensional Circular Cylinder in a Uniform Flow," *Journal of Fluid Mechanics*, Vol. 471, 2002, p. 285–314. doi:10.1017/S0022112002002124.

[19] Williamson, C. H. K., and Prasad, A., "A New Mechanism for Oblique Wave Resonance in the 'Natural' far Wake," *Journal of Fluid Mechanics*, Vol. 256, 1993, p. 269–313. doi:10.1017/S0022112093002794.

[20] Kwon, K., and Choi, H., "Control of Laminar Vortex Shedding Behind a Circular Cylinder Using Splitter Plates," *Physics of Fluids*, Vol. 8, No. 2, 1996, pp. 479–486. doi:10.1063/1.868801.

[21] Inoue, O., and Yamazaki, T., "Secondary Vortex Streets in Two-Dimensional Cylinder Wakes," *Fluid Dynamics Research*, Vol. 25, No. 1, 1999, pp. 1–18. doi:10.1016/S0169-5983(98)00027-6.

[22] Landau, L. D., and Lifshitz, E. M., *Fluid Mechanics*, 2^{nd} ed., Vol. 6, Pergamon Press, 1987.

[23] Cheong, C., Joseph, P., Park, Y., and Lee, S., "Computation of Aeolian Tone From a Circular Cylinder Using Source Models," *Applied Acoustics*, Vol. 69, No. 2, 2008, pp. 110–126. doi:10.1016/j.apacoust.2006.10.004.

[24] Rockwell, D., and Naudascher, E., "Review-Self-Sustaining Oscillations of Flow Past Cavities," *Journal of Fluids Engineering*, Vol. 100, No. 2, 1978, pp. 152–165. doi:10.1115/1.3448624.

[25] Hanna, M., and Mohany, A., "Aeroacoustics and Shear Layer Characteristics of Confined Cavities Subject to Low Mach Number Flow," *Journal of Fluids and Structures*, Vol. 121, 2023, p. 103949. doi:10.1016/j.jfluidstructs.2023.103949.

[26] Mathey, F., Morin, O., Caruelle, B., and Debatim, K., "Simulation of Aeroacoustic Sources in Aircraft Climate Control System," *12th AIAA/CEAS Aeroacoustics Conference (27th AIAA Aeroacoustics Conference)*, 2006. doi:10.2514/6.2006-2493, No.: AIAA-2006-2493.

[27] Mendonca, F., Read, A., Caro, S., Debatin, K., and Caruelle, B., "Aeroacoustic Simulation of Double Diaphragm Orifices in an Aircraft Climate Control System," *11th AIAA/CEAS Aeroacoustics Conference*, 2005. doi:10.2514/6.2005-2976, No.: AIAA-2005-2976.

[28] Belanger, A., Meskine, M., Caruelle, B., and Debatin, K., "Aero-acoustic Simulation of a Double Diaphragm Using Lattice Boltzmann Method," *11th AIAA/CEAS Aeroacoustics Conference*, 2005. doi:10.2514/6.2005-2917, No.: AIAA-2005-2917.

[29] Sovardi, C., and Polifke, W., "Acoustic Characterisation of Double-Orifice Configurations by Means of an LES-SI Approach," *Proceedings of Euronoise 2015*, 2015.

[30] de Reboul, S., Perrey-Debain, E., Ville, J.-M., Zerbib, N., Hugues, F., and Moreau, S., "Experimental and Numerical Observation of Flow-Acoustics Feedback Phenomena due to two Diaphragms in Tandem Inserted in a Rectangular Duct," *Acta Acust.*, Vol. 8, 2024. doi:10.1051/aacus/2023062.

[31] Sengissen, A., Caruelle, B., Souchotte, P., Jondeau, E., and Poinsot, T., "LES of Noise Induced by Flow Through a Double Diaphragm System," *15th AIAA/CEAS Aeroacoustics Conference (30th AIAA Aeroacoustics Conference)*, 2009. doi:10.2514/6.2009-3357, No.: AIAA-2009-3357.

[32] Nicoud, F., and Ducros, F., "Subgrid-Scale Stress Modelling Based on the Square of the Velocity Gradient Tensor," *Flow, Turbulence and Combustion*, Vol. 62, 1999, pp. 183–200. doi:10.1023/A:1009995426001.

[33] Rudy, D. H., and Strikwerda, J. C., "A Nonreflecting Outflow Boundary Condition for Subsonic Navier-Stokes Calculations," *Journal of Computational Physics*, Vol. 36, No. 1, 1980, pp. 55–70. doi:10.1016/0021-9991(80)90174-6.